Journal of Materials Chemistry A

ROYAL SOCIETY OF CHEMISTRY

PAPER

View Article Online
View Journal | View Issue

Cite this: J. Mater. Chem. A, 2025, 13, 25829

Interfacial engineering of Fe–O–Zn bonds in heterojunction photocatalysts: synergistic visible light PMS activation and electron transfer efficiency enhancement†

Peng Chen,[ab] Yuqing Zhao,[ac] Chenyu Li,*[a] Xiaoqi Chen[ad] and Jingfeng Wang *[a]

Traditional Fenton-like catalysts suffer from low efficiency and poor catalytic activity. In this study, Zn-modified α-Fe_2O_3 (FZ13) catalysts were prepared using a hydrothermal method, and their catalytic performance was evaluated for activating peroxymonosulfate (PMS) to degrade tetracycline (TC) under visible light. The results showed that the degradation efficiency of TC in the FZ13 + PMS + light system reached 84% (FZ13: 0.3 g L^{-1}, PMS: 3 mM, TC concentration: 40 mg L^{-1}, temperature: 25 °C, pH: 5.5), with a rate constant (k) of 0.0642 min^{-1}, which is 1.6 times higher than that of the unmodified α-Fe_2O_3 + PMS + light system. The heterojunction structure of FZ13 forms Fe–O–Zn bonds, enhancing electron transport efficiency, approximately 2.17 times that of the unmodified α-Fe_2O_3, and improving the separation of photogenerated electron–hole pairs. Additionally, FZ13 exhibits a high redox capacity, promoting electron transport and charge transfer. DFT calculations confirm that the adsorption energy of FZ13 (−5.826 eV) is higher than that of α-Fe_2O_3 (−4.6 eV), with FZ13 exhibiting metallic characteristics and a more stable hybrid peak further from the Fermi level. In the FZ13 + PMS + light system, the complex FZ13/PMS* is formed, which facilitates electron transfer and promotes the degradation of TC. $SO_4^{\bullet-}$, $^{\bullet}OH$, $O_2^{\bullet-}$, h^+, e^- and $^1O_2$ also co-participate in the TC degradation process. This study offers a feasible strategy for photo-assisted activation of PMS using Fenton-like catalysts.

Received 24th April 2025
Accepted 26th June 2025

DOI: 10.1039/d5ta03221k

rsc.li/materials-a

1. Introduction

The peroxymonosulfate (PMS)-based oxidation process has emerged as a cutting-edge technology for degrading various organic pollutants and mitigating wastewater pollution by generating reactive oxygen species (ROS) and promoting non-radical pathways.[1] Sulfate radicals ($SO_4^{\bullet-}$) and hydroxyl radicals ($^{\bullet}OH$), which are generated by PMS activation, possess high redox potentials ($SO_4^{\bullet-}$: 2.5–3.1 V, $^{\bullet}OH$: 1.8–2.7 V), long half-lives ($SO_4^{\bullet-}$: 30–40 μs, $^{\bullet}OH$: 20 ns), and a wide operational pH range, making them highly effective in pollutant degradation.[2–4] Among existing activation methods, transition metal oxides have shown promising results in PMS activation.

Iron oxides, particularly, have been widely studied for PMS activation due to their low toxicity, low cost, and abundance as the second most common metal on Earth.[5,6] But many defects are exposed with only iron oxide activation of PMS, such as low efficiency, weak catalytic activity, low conversion efficiency from Fe^{3+} to Fe^{2+}/M^{n+} to $M^{(n+m)+}$ (M = other transition metals), poor repeatability after use, *etc.*, which are the limiting factors of the Fenton reaction.[7] Thus, $FeMO_x$ bimetallic catalyst activation of PMS has been proven to be an effective strategy for enhancing its performance. These catalysts promote an increase in the specific surface area, facilitate rapid O–O bond cleavage in PMS, enhance the conversion of Fe^{3+} to Fe^{2+}, and improve electron transfer, while also regulating the adsorption model of reactant molecules.[1,8–11] Furthermore, $FeMO_x$ bimetallic catalysts can enhance the free radical pathway to accelerate the rate of ROS production. Meanwhile, they can also enhance the non-free radical pathway.[12] The barrier of O–O bond breakage in PMS is effectively dropped through the interaction between Fe and M bimetals, thus accelerating the decomposition of the system to produce more singlet oxygen ($^1O_2$), and promoting the O–H bond breakage in PMS to form high-valent metal oxides with Fe/M.[13] In this regard, investigating an outstanding $FeMO_x$ bimetallic catalyst that can remarkably lower the activated PMS

[a]Military Medical Sciences Academy, Academy of Military Sciences, Tianjin, 300050, China. E-mail: wangjingfeng0116@163.com; lcy710430@163.com
[b]School of Chemistry and Chemical Engineering, Chongqing University of Technology, Chongqing 400054, China
[c]Department of Toxicology and Health Inspection and Quarantine, School of Public Health, Tianjin Medical University, Tianjin 300070, China
[d]Tianjin Key Laboratory of Pulp and Paper, Tianjin University of Science and Technology, Tianjin, 300457, China

† Electronic supplementary information (ESI) available. See DOI: https://doi.org/10.1039/d5ta03221k

barrier, or increase ROS generation and enhance non-free radical pathways is a decisive task.

Recently, coupling photo-assisted activation of PMS has been proposed as an effective strategy for enhancing pollutant degradation. The electron transfer rate under visible light determines the efficiency of ROS generation during PMS activation.[14] Visible light stimulation increases electron generation, thereby improving PMS activation performance.[15,16] Furthermore, PMS acts as an electron acceptor, enhancing the separation and transfer of photoexcited carriers, which maximizes the utilization of both PMS and catalysts.[17] ZnO_x has been widely studied for its visible light photocatalytic properties.[18,19] However, ZnO_x's wide band gap structure and high carrier recombination rate limit its efficiency as a PMS activator.[20] These drawbacks hinder the practical application of ZnO_x in PMS activation.[21] Combining ZnO_x with FeO_x to form a heterojunction structure has been shown to improve photocatalytic performance and enhance PMS activation activity.[22,23] Heterojunctions improve electron transfer in photo-assisted PMS activation systems, facilitate the separation of photogenerated electron–hole pairs, and increase the specific surface area of composites while reducing the metal ion leaching rate.[24,25]

Inspired by these findings, α-Fe_2O_3 was modified by introducing a Zn precursor (FZ13) through a hydrothermal method in this study. The catalytic performance of these materials was evaluated for tetracycline (TC) degradation *via* PMS activation under visible light. The role of Zn modification in enhancing the photo-assisted activation of PMS by FZ13 was explored, and the mechanism behind TC degradation in the FZ13 + PMS + light system was elucidated. Finally, the broad applicability of the FZ13 + PMS + light system was discussed.

2. Experimental

2.1 Reagents and methods

All reagents are analytical grade. Details of the reagents and methods used are provided in S1 and S2.†

2.2 Characterization

The performance of the catalyst is evaluated by characterization. The methods are described in S3.†

2.3 DFT calculations

The adsorption energy, differential charge density (DCD), and density of states (DOS) of the catalyst were investigated through DFT calculations. Detailed information regarding the DFT calculations is presented in S4.†

2.4 Catalyst preparation

The preparation method for α-Fe_2O_3 is outlined in S5.†

The synthesis steps of Fe/Zn bimetallic catalysts are as follows. 1.365 g of $FeCl_3 \cdot 6H_2O$, 2.789 g of CH_3COONa, and varying amounts of $Zn(CH_3COO)_2 \cdot 2H_2O$ were added to a 93.3% 50 mL ethanol solution. The pH of the mixed solution is approximately 4. The mixture was stirred for 30 minutes until it became homogeneous (rotational speed: 200–250 rpm). Then, the solution was transferred to a homogeneous reactor and hydrothermally treated at 180 °C for 12 hours. After the reaction, the mixture was cooled to room temperature, washed several times with deionized water and anhydrous ethanol, and dried in an oven at 60 °C for 12 hours to obtain the catalyst. The resulting Fe/Zn bimetallic catalysts were named based on the molar ratio of Fe to Zn (*e.g.*, FZ*XX*), with the specific samples being labeled FZ31, FZ21, FZ11, FZ12, FZ13, and FZ14.

2.5 Experimental procedure

All experiments were conducted in a 500 mL beaker containing the solution to be degraded. Two LED lamps were positioned around the beaker to irradiate the solution with visible light (wavelength λ = 405 nm, light intensity = 24 μmol m^{-2} s^{-1}). During the reaction, 2 mL samples were withdrawn at regular intervals and filtered using a 0.22 μm polyether sulfone membrane filter to determine the absorbance.

The catalytic performance was initially evaluated through characterization, control experiments, and cycling experiments. The reaction mechanism was further elucidated through quenching experiments, electrochemical tests, and DFT calculations. Finally, possible reaction pathways and the toxicity of intermediate products were investigated using LC-MS and the Toxicity Estimation Software Tool (T.E.S.T.).

The composition of the electron-coupled oxidation system (GOS) is shown in S6.†

3. Results and discussion

3.1 Characterization

The preparation process of the FZ13 catalyst is shown in Fig. 1(a). The morphology of the α-Fe_2O_3 catalyst appears as elliptical disks (Fig. 1(b) and (c)). In contrast, the FZ13 catalyst exhibits an irregular morphology with a porous structure, and its surface changes from smooth to rough, as observed in Fig. 1(d) and (e). The elemental mapping images (Fig. 1(f)–(i)) confirm the uniform distribution of C, Fe, O, and Zn in the FZ13 catalyst.

Further analysis was conducted through TEM and HRTEM to investigate the differences between α-Fe_2O_3 and FZ13, their morphology, corresponding crystal planes, and plane spacing under high magnification. α-Fe_2O_3 also appears in an elliptical disk under high magnification, consistent with the SEM results. The α-Fe_2O_3 plane is 0.25 nm, and it is proved to be the (110) crystal plane, as shown in Fig. S1(a) and (b).† TEM was performed to observe the morphology of FZ13, and it is found to be granular, which is consistent with SEM results (Fig. 1(j)). Furthermore, its possible reaction crystal planes are analyzed *via* HRTEM, as displayed in Fig. 1(k) and (l). The spacing between the two typical crystal planes is 0.24 nm and 0.26 nm, which is closely related to the ZnO(101) crystal plane and $FeCO_3$(104) crystal plane.

The crystal structure of the prepared catalyst was characterized by XRD, as displayed in Fig. 2(a). Two distinct characteristic peaks of α-Fe_2O_3 are detected at 34.98° and 61.66°, matching the Fe_2O_3 phase (JCPDS no. 33-0664). For the FZ13 composite

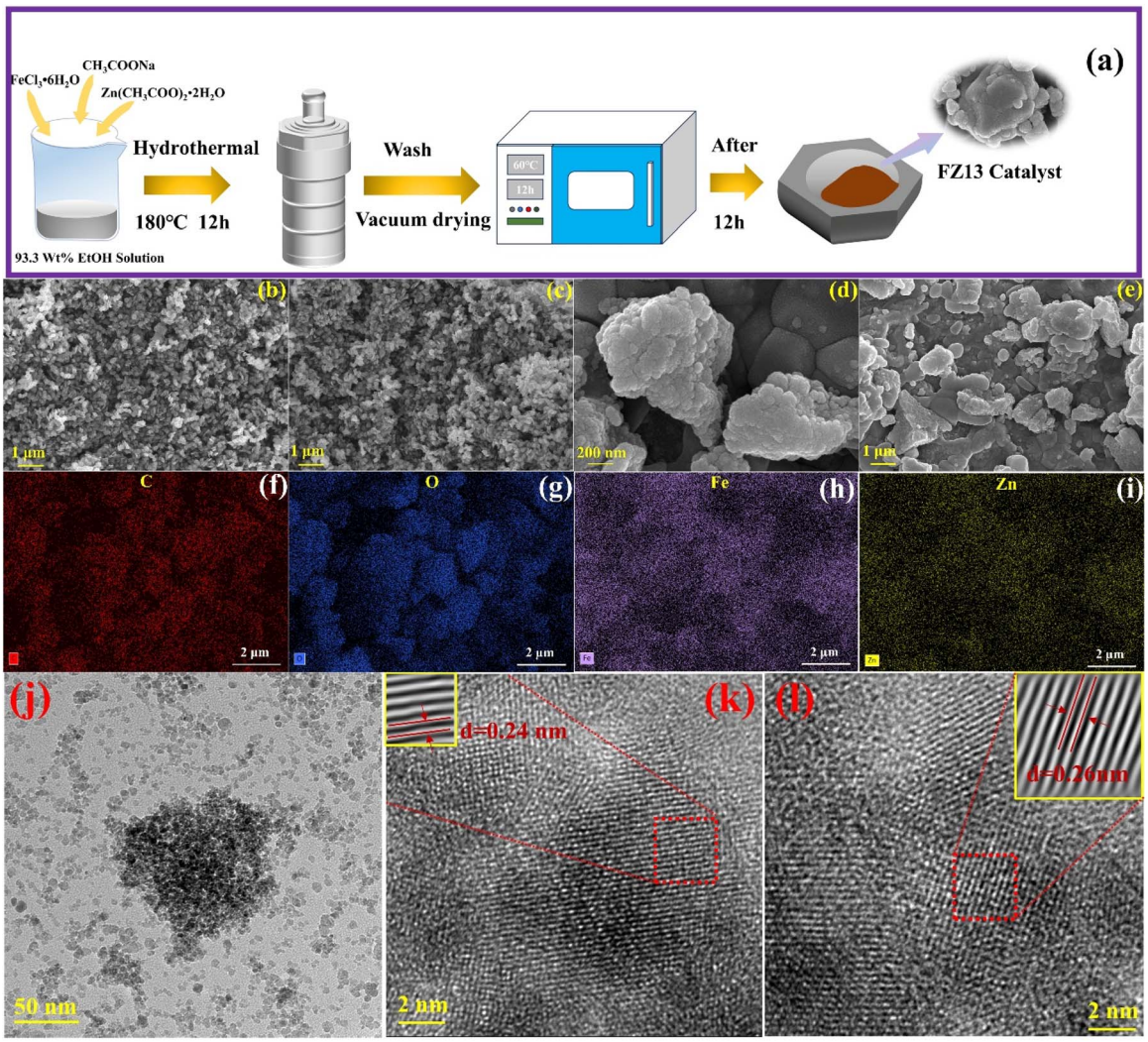

Fig. 1 (a) FZ13 catalyst preparation process; (b and c) SEM of α-Fe_2O_3; (d and e) SEM of FZ13; (f–i) mapping images of FZ13; (j) TEM and (k and l) HRTEM of FZ13.

catalysts prepared by the hydrothermal method, Zn modification leads to notable changes in the phase structure of the original catalyst. Specifically, distinct peaks appear at 31.88°, 36.6°, 45.8°, 56.92°, 66.46° and 75.48° for FZ13 composites, which are attributed to $FeCO_3$(104), ZnO(101), Fe(111), ZnO(110), ZnO(200), $FeCO_3$(217) crystal planes, respectively.

Additionally, the functional groups of different materials were detected by FT-IR (Fig. 2(b)). For α-Fe_2O_3, a characteristic tensile vibration peak is observed between 400 and 650 cm^{-1}, corresponding to the Fe–O bond. The FZ*XX* composite materials exhibit characteristic peaks at approximately 3440 cm^{-1}, 1570 cm^{-1}, and 1430 cm^{-1}, which are related to the H–O–H and O–H bonds of adsorbed water on the surface.[26] The tensile vibration peaks between 400 cm^{-1} and 600 cm^{-1} belong to the Fe–O–Zn bond.[7,27]

The chemical states of α-Fe_2O_3 and FZ13 were further researched by XPS, as demonstrated in Fig. 2(c). The XPS spectrum reveals a new peak at 1020 eV for FZ13, corresponding to Zn 2p, which is absent in α-Fe_2O_3. In comparison to the Fe 2p high-resolution spectrum, the Fe $2p_{1/2}$, Fe $2p_{3/2}$ and satellite peaks in FZ13 shift, as displayed in Fig. 2(d). Notably, FZ13 has a small but distinct peak at 710.2 eV, which is assigned to Fe^0, indicating the partial reduction of Fe^{3+} under the influence of the heterojunction.[28] This is attributed to increased local electron density due to the Fe–O–Zn bond environment, which facilitates electron transfer and results in the partial conversion of Fe^{3+} to Fe^{2+} and Fe^0 to maintain charge neutrality.[29] Compared with pristine α-Fe_2O_3, FZ13 exhibits a higher Fe^{2+}/Fe^{3+} ratio and the emergence of Fe^0, implying enhanced redox activity. These reduced iron species (Fe^{2+} and Fe^0) are known to act as active sites for PMS activation, promoting radical generation and improving catalytic performance.[30]

To understand the effect of Zn modification on the catalytic performance of the composites, N_2 adsorption–desorption isothermal curves were analyzed to evaluate the specific surface area and mesoporosity of different materials. As depicted in Fig. S2(a)–(g) and Table S1,† the specific surface area of the FZ*XX* composites increases, while the pore volume and average pore diameter decrease to varying extents after Zn modification, suggesting a high number of oxygen vacancies in the

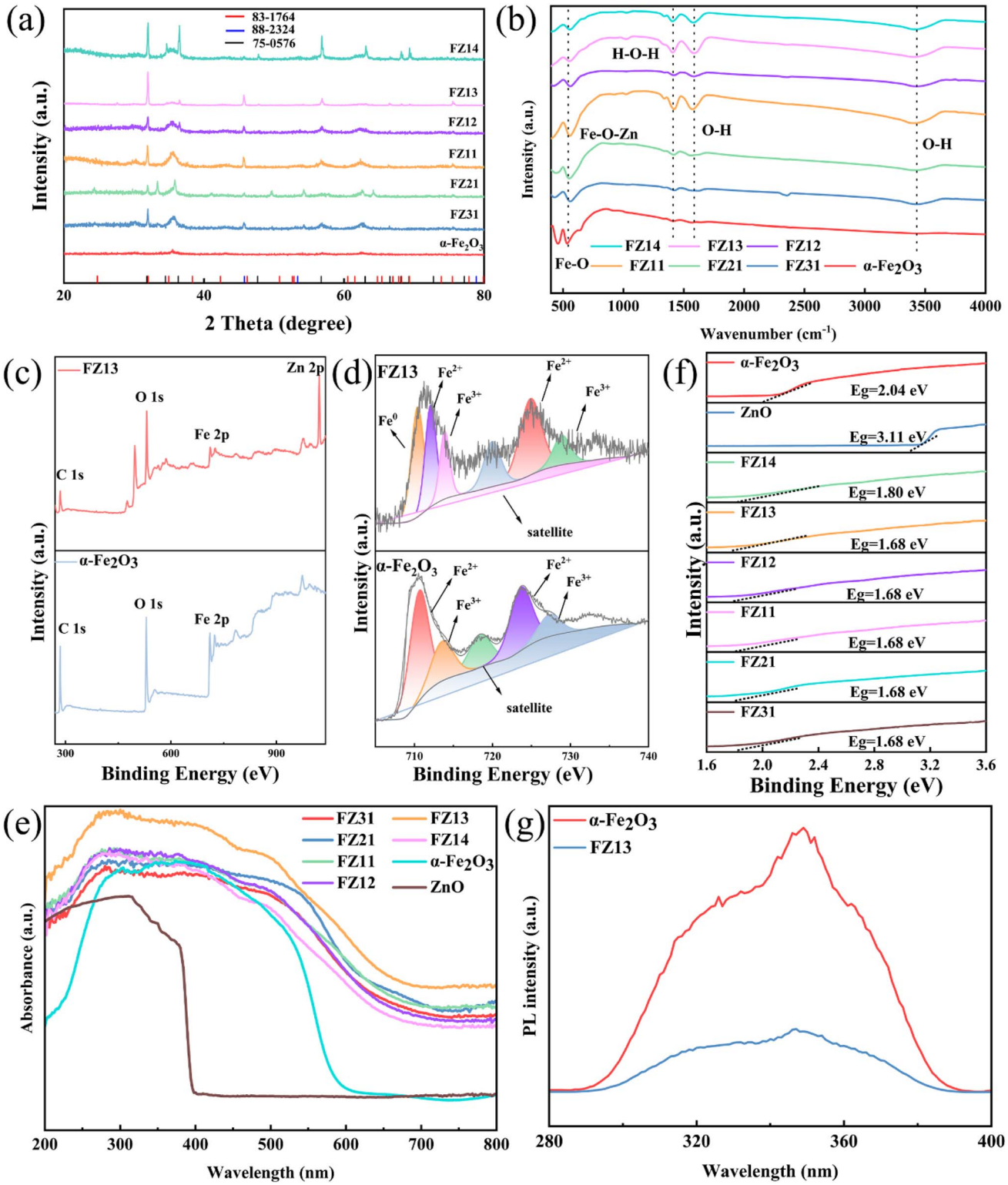

Fig. 2 (a) XRD patterns of α-Fe_2O_3 and FZ31–FZ14; (b) FT-IR spectra of α-Fe_2O_3 and FZ31–FZ14; (c) XPS spectra of α-Fe_2O_3 and FZ13; (d) Fe 2p high-resolution XPS spectra of α-Fe_2O_3 and FZ13; (e) UV-vis of α-Fe_2O_3, ZnO and FZ31–FZ14; (f) E_g values of α-Fe_2O_3, ZnO and FZ31–FZ14; (g) PL spectra.

composites. Besides, the adsorption–desorption isotherms of all materials exhibit a type IV isotherm with H3 hysteresis loops. It means that the above catalysts are mesoporous with irregular pore structures since there is no obvious saturation plateau for adsorption.[31] The larger specific surface area facilitates more active adsorption sites for redox reactions, which improves the photocatalytic performance. Notably, in the photo-assisted PMS activation co-degradation system, the specific surface area is

a secondary factor; the free radicals generated by photogenerated electron holes are the primary contributors to performance.[32]

The performance of the catalyst in activating PMS is closely linked to its optical properties and electron migration.[32] Therefore, the optical properties were examined. Metal doping and defect structures generally enhance the photoabsorption properties of composite materials. As shown in Fig. 2(e), the FZ*XX* composite demonstrates stronger absorption than α-Fe_2O_3/ZnO in the visible light range (200–800 nm), with FZ13 exhibiting the widest absorption range. This can be attributed to the formation of heterojunctions, which enhance the ability of FZ13 to efficiently absorb visible light photons.[18]

Simultaneously, the energy band gap (E_g) of different materials was calculated to reflect their photocatalytic properties. As illustrated in Fig. 2(f), the heterojunction formed by FZ13 causes a redshift in the absorption edge (E_g 1.68 eV) compared to the original α-Fe_2O_3 (E_g 2.04 eV). This redshift facilitates the generation of more free electrons under visible light irradiation, thus promoting efficient PMS activation and improving the composite materials' visible light utilization efficiency.[33,34]

PL was used to analyze the separation efficiency of photogenerated electron–hole pairs in the different materials, as shown in Fig. 2(g). α-Fe_2O_3 produces a strong PL emission peak near 350 nm, which is attributed to the recombination of photogenerated electron–hole pairs.[35] The peak intensity for the FZ13 composite is significantly reduced after Zn modification, indicating enhanced carrier separation and transfer. The resulting heterojunction structure improves electron–hole separation efficiency, while Zn modification shortens the electron transfer path and accelerates the movement of photogenerated electrons and holes.[36,37]

These results collectively indicate that both surface and interfacial properties of the FZ13 catalyst play crucial roles in enhancing its photocatalytic performance. The SEM and TEM images show that the surface of FZ13 transforms from smooth elliptical disks to a rough, porous texture, which increases the number of active sites and facilitates better adsorption of PMS and pollutants such as TC. Meanwhile, the formation of Fe–O–Zn bonds at the heterojunction interface effectively enhances interfacial charge separation and transfer. These bonds serve as electron bridges that reduce the recombination of photogenerated carriers, as evidenced by the significantly reduced PL intensity and smaller arc radius in the EIS spectra. Furthermore, the heterojunction formed between FZ13 results in appropriate band alignment and internal electric fields, which promote the directional migration of electrons and holes under visible light irradiation. Therefore, the synergistic effect of the optimized surface morphology and the interfacial electronic structure leads to improved light harvesting, more efficient PMS activation, and enhanced overall catalytic performance.[26]

3.2 Comparison of catalytic performance

First, the catalytic performance of FZ*XX* catalysts with different Fe/Zn molar ratios in the FZ*XX* + PMS + light system is investigated, as plotted in Fig. 3(a) and (b). The FZ*XX* bimetallic catalyst demonstrates excellent catalytic activity at a Fe/Zn molar ratio of 1 : 3 (FZ13), with the reaction rate constant k increasing from 0.028 min^{-1} to 0.0662 min^{-1}. This improvement can be attributed to the promotion of the non-radical pathway as the Zn content increases, which accelerates the degradation of TC. However, when the Zn content is further increased (Fe : Zn = 1 : 4), the TC degradation efficiency slows down, as Zn inhibits the catalytic activity of Fe.

The catalytic performance of various systems is systematically assessed through two key indicators: TC oxidative degradation and reaction rate constant k, as displayed in Fig. 3(c)–(e). In the PMS-only system, a modest TC degradation efficiency of 33% is observed, attributable to the absence of catalyst–PMS interaction required for generating active sites. This insufficient ROS generation consequently results in sluggish TC degradation kinetics. Notably, both the FZ13 + PMS (dark condition) and FZ13 + light (PMS-free) systems exhibit unsatisfactory performance, highlighting the essential synergistic effect between light irradiation and PMS activation for effective TC degradation.[36] The FZ13 + PMS + light system demonstrates remarkable superiority, achieving 84% TC degradation efficiency with a reaction rate constant of 0.0642 min^{-1}. This performance significantly outperforms both the unmodified α-Fe_2O_3 + PMS + light system and single metal oxide systems (ZnO/$FeCO_3$/Fe + PMS + light). Meanwhile, the adsorption capacity of FZ13 is higher than that of α-Fe_2O_3, further highlighting its excellent performance (Fig. S3†). Additional validation of the FZ13 system's efficiency is provided by comparative analyses of PMS consumption and total organic carbon (TOC) removal, which reached 56.67%, as quantified in Fig. 3(h) and (i) and summarized in Table S2.†

The reusability of catalytic materials constitutes a critical practical criterion encompassing environmental sustainability and operational stability. The FZ13 catalyst maintains remarkable consistency in TC degradation efficiency through five consecutive catalytic cycles, providing compelling evidence for its structural robustness and catalytic durability (Fig. 3(f)). Furthermore, the leaching concentration of Fe and Zn ions was monitored using ICP, as depicted in Fig. 3(g). The leaching rate of both metal ions gradually stabilized as the number of cycles increased (detailed Fe/Zn ion leaching concentrations are provided in Table S3†). Further characterization of FZ13 before and after the reaction by FT-IR, XRD and UV-vis spectroscopy (Fig. S4–S6†) confirms that the phase structure of the catalyst remains largely unchanged. Its excellent cyclability and structural stability significantly reduce the environmental impact over the entire life cycle. Compared with conventional catalytic systems, the approach proposed in this study offers distinct advantages in terms of environmental footprint and aligns closely with the principles of sustainable technology. This study compared the performance of various catalysts in activating PMS for the degradation of TC, highlighting the superior efficiency of the FZ13 + PMS + light system, as presented in Table S4.†

Additionally, the effects of individual factors on the degradation efficiency of TC were investigated, as illustrated in Fig. S7(a)–(d).† As shown in Fig. S7(a),† increasing the catalyst

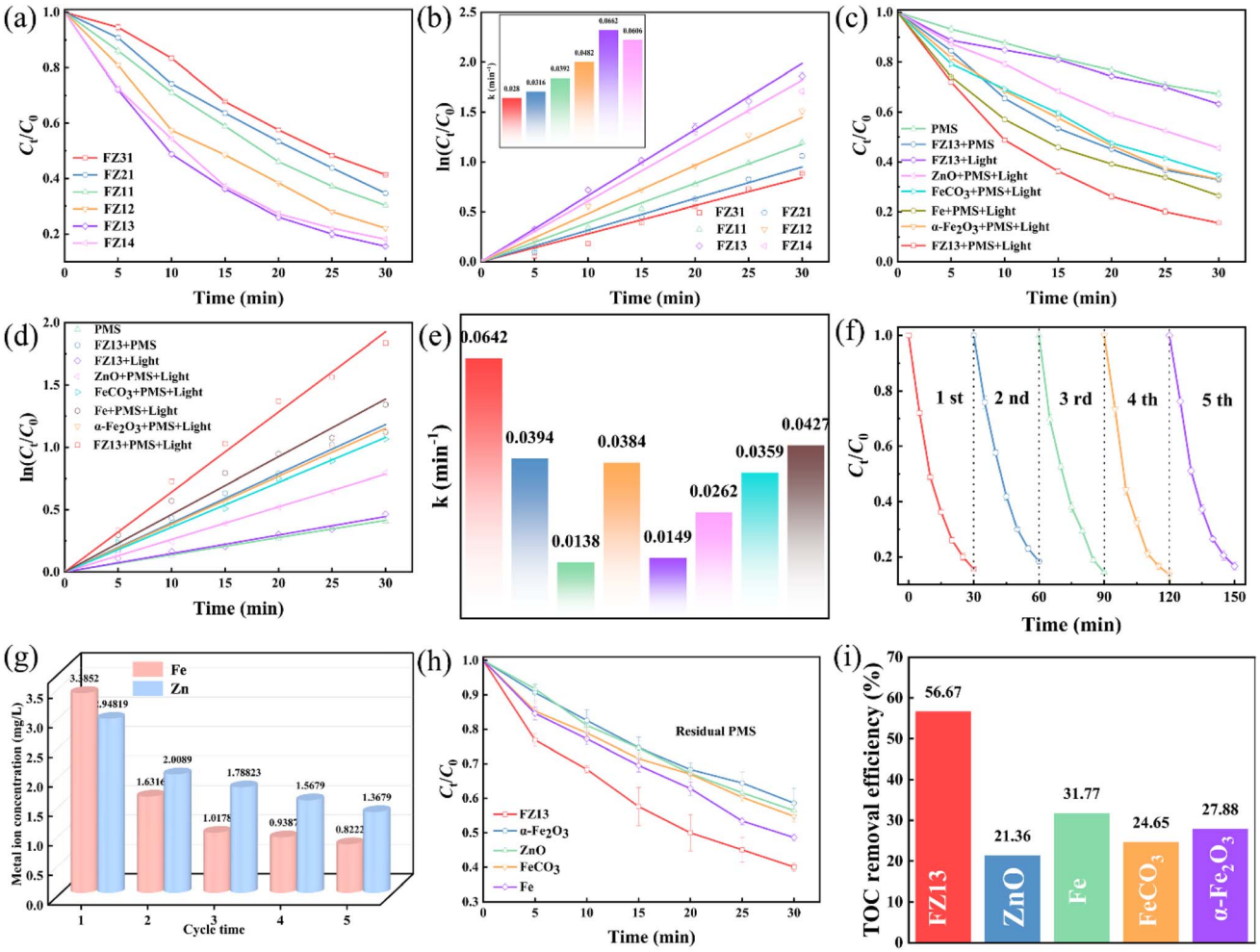

Fig. 3 (a) Degradation efficiency of TC with different molar ratios of Fe and Zn; (b) the fitted first-order reaction kinetics and rate constant *k* of Fe and Zn with different molar ratios; (c) the degradation efficiency of TC in different systems; (d) fitting its first-order dynamics; (e) its corresponding reaction rate constant *k*; (f) cycle experiment; (g) ICP detection of metal ion leaching with different cycle times; (h) PMS consumption rate; (i) TOC removal efficiency. (experimental parameters: catalyst: 0.3 g L^{-1}; PMS: 3 mM; TC: 300 mL, 40 mg L^{-1}; temperature: 25 °C; pH: 5.5.)

concentration from 0 to 0.4 g L^{-1} initially enhances the TC degradation efficiency, which then reaches a plateau. This behavior can be attributed to the catalyst providing sufficient active sites for the reaction, thereby generating more ROS and facilitating TC degradation. The efficiency levels off due to the limited availability of PMS in the reaction system and the finite adsorption capacity of the catalyst.

Similarly, Fig. S7(b)† shows that the degradation efficiency of TC increases with the PMS concentration from 0 to 5 mM before stabilizing. This trend arises because higher PMS concentrations produce more $SO_4^{\bullet-}$; however, excessive PMS can quench these radicals, thereby reducing their effective concentration.

The influence of the initial TC concentration and reaction temperature on degradation efficiency is presented in Fig. S7(c) and (d),† respectively. As the initial concentration of TC increases, the degradation rate decreases. This is due to the fixed amount of ROS in the system, which becomes insufficient to degrade the higher number of TC molecules. In contrast, higher reaction temperatures significantly enhance TC degradation. This can be explained by the accelerated molecular motion at elevated temperatures, which promotes more frequent and effective collisions among reactants.

3.3 Reaction mechanism

3.3.1 Identification of ROS and non-free radical pathways. To elucidate the ROS generation mechanism in the FZ13 + PMS + light system, systematic quenching experiments were performed, as presented in Fig. 4(a). *tert*-Butanol (TBA) is selected to quench $^{\bullet}OH$, and methanol (MeOH) quenches $^{\bullet}OH$ and $SO_4^{\bullet-}$.[38,39] Notably, the inhibitory effect of MeOH is somewhat stronger than that of TBA at the two concentrations of 0.3 M and 0.6 M. This is because TBA, being more hydrophobic, is more likely to occupy the catalyst surface, hindering the adsorption and activation of PMS.[8] This also identifies that $SO_4^{\bullet-}$ plays a dominant role in the oxidative degradation of TC.

Additionally, ascorbic acid (AA) and L-tryptophan (L-Tp) are selected as quenchers of $O_2^{\bullet-}$ and $^1O_2$.[7,40] As illustrated in Fig. 4(a) and (b), the radical pathway involving $SO_4^{\bullet-}$, $^{\bullet}OH$ and

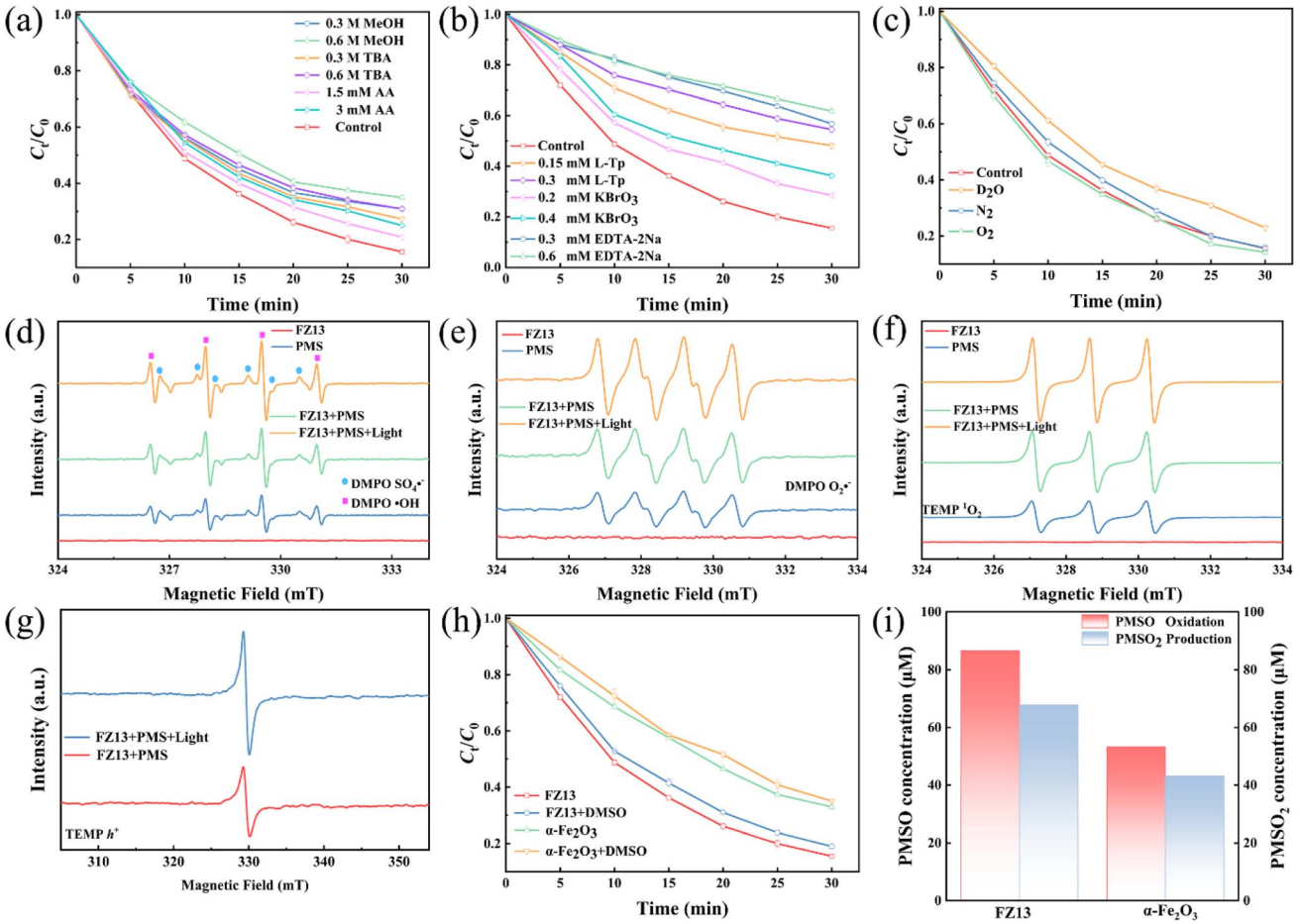

Fig. 4 Quenching experiments (a–c); (d) $SO_4^{\bullet-}$ and $^{\bullet}OH$ EPR; (e) $O_2^{\bullet-}$ EPR; (f) $^1O_2$ EPR; (g) oxygen vacancy; (h) DMSO quenching experiments; (i) PMSO quenching experiments.

$O_2^{\bullet-}$ contributes minimally to the degradation of TC when compared to $^1O_2$. The inhibitory effect on TC degradation increases significantly with rising concentrations of L-Tp, indicating that $^1O_2$ plays a crucial role in TC degradation. Gas-phase control experiments further corroborate this mechanism insensitivity of TC degradation efficiency to the N_2/O_2 atmosphere, confirming that $^1O_2$ generation originated intrinsically from the catalytic system[41] (Fig. 4(c)). Deuterium isotope effects in heavy water (D_2O) solvent (Fig. 4(c)) provide additional mechanistic validation, demonstrating marked reaction rate suppression due to $^1O_2$ production inhibition.[42]

Ethylenediaminetetraacetic acid disodium salt (EDTA-2Na) can act as a quencher of holes (h^+).[43,44] As plotted in Fig. 4(b), the degradation of TC drops instantly after adding EDTA-2Na, indicating that h^+ has a huge contribution to the degradation of TC. The reason for this is that EDTA anions adhere to the surface of the FZ13 catalyst and can act as h^+ traps or electron donors, resulting in the inhibition of catalyst photocatalytic performance.[45] Furthermore, it is also because EDTA-2Na prevents h^+ from reacting with water to further generate $^{\bullet}OH$.[2]

As shown in Fig. 4(d)–(f), the ROS content of different systems was detected such as FZ13, PMS, FZ13 + PMS, and FZ13 + PMS + light. Interestingly, the signal intensity of the FZ13 + PMS + light system is much higher than that of the first three. This is attributed to FZ13 producing sufficient ROS under the synergistic effect of the photocatalyst and PMS. Meanwhile, the intensity of oxygen vacancies in different systems is observed respectively, as shown in Fig. 4(g). The signal intensity is stronger in the FZ13 + PMS + light system, and the results show that the introduction of visible light improves the generation of e^- and h^+ and promotes the formation of defect sites.

In transition metal oxide-activated PMS systems, high valence metal oxides (HVMOs) have been proven to contribute to the degradation of pollutants.[46] To explore the role of HVMOs, dimethyl sulfoxide (DMSO) was introduced as a probe (Fig. 4(h)). After DMSO addition, the TC degradation efficiency decreases by 7% in the FZ13 + PMS + light system, while that in the unmodified α-Fe_2O_3 + PMS + light system declines by 3%. This suggests that the effect of HVMOs on TC degradation in this system is minimal. Furthermore, the participation of HVMOs in TC degradation was further evaluated by methyl phenyl sulfoxide (PMSO) oxidation and $PMSO_2$ production, as shown in Fig. 4(i). Approximately 20% of PMSO is consumed to produce sulfones ($PMSO_2$) in the FZ13 + PMS + light system, suggesting that there is a trace amount of HVMOs in the system.[6] Overall, the quenching experiments indicate that

HVMOs have a minor role in TC degradation, with the process primarily driven by free radicals and other non-radical pathways.

3.3.2 Electron transfer pathway. Considering that electron transfer occurs during TC degradation in the FZ13 + PMS + light system, a high-performance electron quencher ($KBrO_3$) was selected for verification. As shown in Fig. 4(b), the degradation efficiency of TC is significantly inhibited after the addition of $KBrO_3$, indicating that electron transfer plays a crucial role in the degradation of TC.

To further elucidate the electron transfer mechanism, an electron-coupled oxidation system (GOS) was set up to ensure that TC degradation occurs solely *via* the electron transfer pathway (Fig. 5(a)). The current indicators reach peak values at 0 min for all systems (FZ13 + light 0 μA, PMS + light 10.5 μA, α-Fe_2O_3 + PMS + light 57 μA, and FZ13 + PMS + light 124 μA), after which a general decline is observed (Fig. 5(b)). Notably, no change in the current indicator is observed in the two systems with only the FZ13 catalyst and PMS. This provides strong evidence that TC degradation supplies electrons to PMS *via* the catalyst (acting as an electronic medium), rather than directly.[47]

Furthermore, the highest current in the FZ13 + PMS + light system suggests that Zn modification enhances the charge transfer ability of the catalyst, compared to the unmodified α-Fe_2O_3 catalyst. This further confirms that electron transfer occurs in the degradation of TC in this system.

The EIS results of α-Fe_2O_3, ZnO and FZ13 catalysts were analyzed, as shown in Fig. 5(c). Interestingly, FZ13 shows the smallest EIS arc radius, confirming its superior charge transfer rate.[48] The heterojunction structure in FZ13 effectively reduces internal resistance.

The electron transfer properties of the three materials were further evaluated using photoelectrochemical measurements, as depicted in Fig. 5(d). The FZ13 composite exhibits the highest current under visible light irradiation, indicating minimal internal resistance, faster electron transfer, and higher charge transfer efficiency.[49] Additionally, the strong photocurrent intensity of FZ13 is attributed to the Fe–O–Zn bond, which dominates the electron transport process. In contrast, the unmodified ZnO/α-Fe_2O_3 shows poor visible light absorption.

The activation of PMS by different catalysts involves a charge transfer process, which was investigated using CV. As illustrated

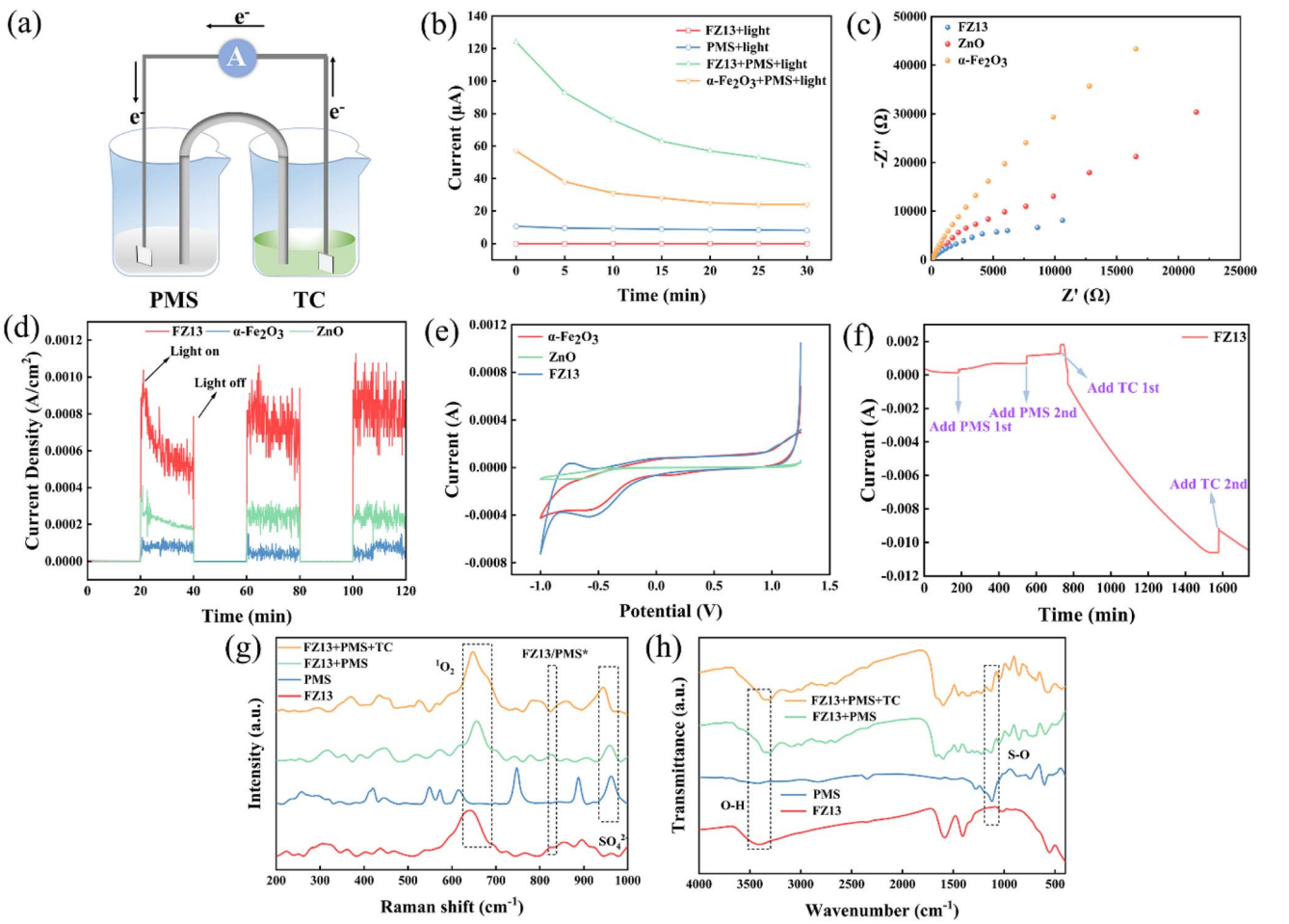

Fig. 5 (a) Electron-coupled oxidation system (GOS); (b) current variation of different systems in the GOS system; (c) EIS Nyquist plots of α-Fe_2O_3, ZnO and FZ13; (d) transient photocurrent responses of α-Fe_2O_3, ZnO and FZ13; (e) CV curves of α-Fe_2O_3, ZnO and FZ13, (f) *i*–*t* curves, (g) Raman spectra, (h) FT-IR spectra.

in Fig. 5(e), FZ13 has the largest integral area, indicating the greatest capacitance and the ability to transfer and store more electrons. Meanwhile, FZ13 exhibits the highest current density, suggesting that the valence transfer rate of Fe/Zn is faster, enhancing the redox process during PMS activation.

An open circuit potential (OCP) test was conducted to monitor the electron transfer process after adding PMS and TC, as plotted in Fig. 5(f). The potential increases significantly after two additions of PMS, which is attributed to the redistribution of electron density in the working electrode caused by PMS adsorption, and the formation of the FZ13/PMS* complex with a high redox reaction in the system.[50] The potential of the system increases slightly at first after adding TC, but then rapidly decreases after the second addition of TC. The initial increase is due to the redox potential of the FZ13/PMS* complex being elevated by TC, while the subsequent decrease is due to TC consumption of the FZ13/PMS* complex, leading to a decline in potential.[49] These results indicate strong electron transfer between TC and FZ13/PMS* in the FZ13 + PMS + light system, providing strong evidence for TC degradation through electron transfer in this system.

The reaction process in the FZ13 + PMS + light system was further investigated using Raman spectroscopy, as plotted in Fig. 5(g). Distinct peaks at 650 cm^{-1} and 960 cm^{-1} become more intense due to the adsorption of SO_4^{2-} and the generation of $^1O_2$ during PMS activation.[51] Additionally, a new peak at 830 cm^{-1} in the FZ13 + PMS system appears compared to the PMS and FZ13-only systems, which is related to the formation of the FZ13/PMS* complex.[52] The peak intensity weakens in the FZ13 + PMS + TC system, indicating that the FZ13/PMS* complex is consumed during TC degradation. This also confirms that the FZ13/PMS* complex is one of the active species responsible for TC degradation.

As depicted in Fig. 5(h), the peak near 3400 cm^{-1} in FZ13 is attributed to O–H vibrations, while shifts in the O–H stretching vibrations in the FZ13 + PMS and FZ13 + PMS + TC systems provide strong evidence for the formation of FZ13/PMS* complexes.[31] For PMS, a characteristic peak at 1130 cm^{-1} corresponds to the S–O bond. Similarly, the S–O bond is shifted in the FZ13 + PMS and FZ13 + PMS + TC systems, indicating that the interaction between the FZ13 catalyst and PMS causes electron rearrangement and weakens the electron density of the S–O bond. This is direct evidence of the formation of FZ13/PMS* complexes in the system.[53]

More importantly, the chemical state changes of C, O, Fe and Zn were investigated by XPS to explore the electron transfer mechanism in the FZ13 + PMS + light system. As shown in Fig. S8(a),† the full spectrum of XPS remains uncharged, so a closer examination of the fine spectrum is necessary. Fig. S8(b)† shows C 1s, corresponding to three types of bonds: C–C/C=C, C=O, and –COOH. The content of these bonds does not change before and after the reaction. The O 1s spectrum, depicted in Fig. S8(c),† exhibits notable changes. The components of O 1s, such as metal oxide (O_2^-), adsorption of water (H_2O), and metal surface hydroxyl group (–OH), show that after the reaction, O_2^- decreases from 23.5% to 14.29%, while H_2O increases from 20.04% to 27.46%. This can be explained by the consumption of the Fe–O–Zn bond during the reaction and strong hydroxylation. Fig. S8(d)† displays two characteristic peaks of Zn 2p located at 1021.78 eV and 1044.93 eV, corresponding to Zn^{2+} in the FZ13 samples. The shifts in these peaks after PMS activation suggest that Zn^{2+} is involved in activating PMS. Zn^{2+} also has high metal activity and can effectively reduce Fe^{3+} to Fe^{2+}, promoting the redox reaction of iron during PMS activation. The fine spectrum of Fe 2p (Fig. S8(e)†) shows a slight decrease in Fe^0 and Fe^{2+}, while the Fe^{3+} content increases. This suggests that PMS activation leads to the oxidation of Fe^{2+} to Fe^{3+}, but the heterojunction in FZ13 helps maintain the internal electron balance and stability.

3.3.3 DFT calculations. The FZ13 composite material, prepared through our modification, exhibits significantly stronger PMS adsorption performance than the original α-Fe_2O_3. The corresponding DFT calculations reveal the underlying mechanism behind this enhancement.

The adsorption of PMS on the catalyst surface is a prerequisite for electron transfer to occur internally, so we first compare the adsorption energy.[54] As displayed in Fig. S9(a),† the adsorption energy of unmodified α-Fe_2O_3 is −4.6 eV, consistent with our previous study.[2] After modification, the adsorption energy of FZ13 increases to −5.826 eV, indicating that FZ13 is more favorable for PMS adsorption (Fig. 6(a)).

DCD is used to further analyze PMS adsorption. In the DCD, cyan regions represent areas where electrons are lost, while yellow regions show areas where electrons are gained. The electron enrichment ability of α-Fe_2O_3 is relatively weak, as shown in Fig. S9(b).† In contrast, FZ13 exhibits strong electron conductivity, which facilitates electron transport (Fig. 6(b)). After PMS adsorption, oxygen vacancies (O_v) appear on the surface, which further enhances adsorption.[55] Additionally, PMS chemisorption is evident at the heterojunction of FZ13, indicating a significant electron transfer phenomenon between Fe and Zn.[56] These results provide clear evidence that heterojunctions and O_v enhance the conductivity and charge transfer capacity during electrochemical processes.[55] As a supplement, O_v can further accelerate the charge transfer efficiency in heterojunction catalysts.

Next, we investigate the differences between α-Fe_2O_3 and FZ13 through DOS analysis, as well as electronic changes at their interface, as shown in Fig. 6(c) and S9(c)† (Fig. 6(d) provides an enlarged view of Fig. 6(c)). α-Fe_2O_3 exhibits semimetallic properties, while FZ13 shows metallic properties, indicating that FZ13 has superior electronic conductivity compared to α-Fe_2O_3. The range of O atoms adsorbed by FZ13 on PMS is wider, deeper, and more stable than the electron distribution on α-Fe_2O_3. Simultaneously, the hybridization peak between PMS and FZ13 is further from the Fermi level than that of α-Fe_2O_3, suggesting greater stability. The shift of the hybridization peak towards the right is due to the lower electron energy and increased conductive carriers.[57] This also explains why the adsorption energy of the modified FZ13 is higher than that of α-Fe_2O_3. These findings demonstrate that the successful construction of heterojunctions significantly promotes carrier concentration, thereby enhancing the catalytic performance of FZ13.[58]

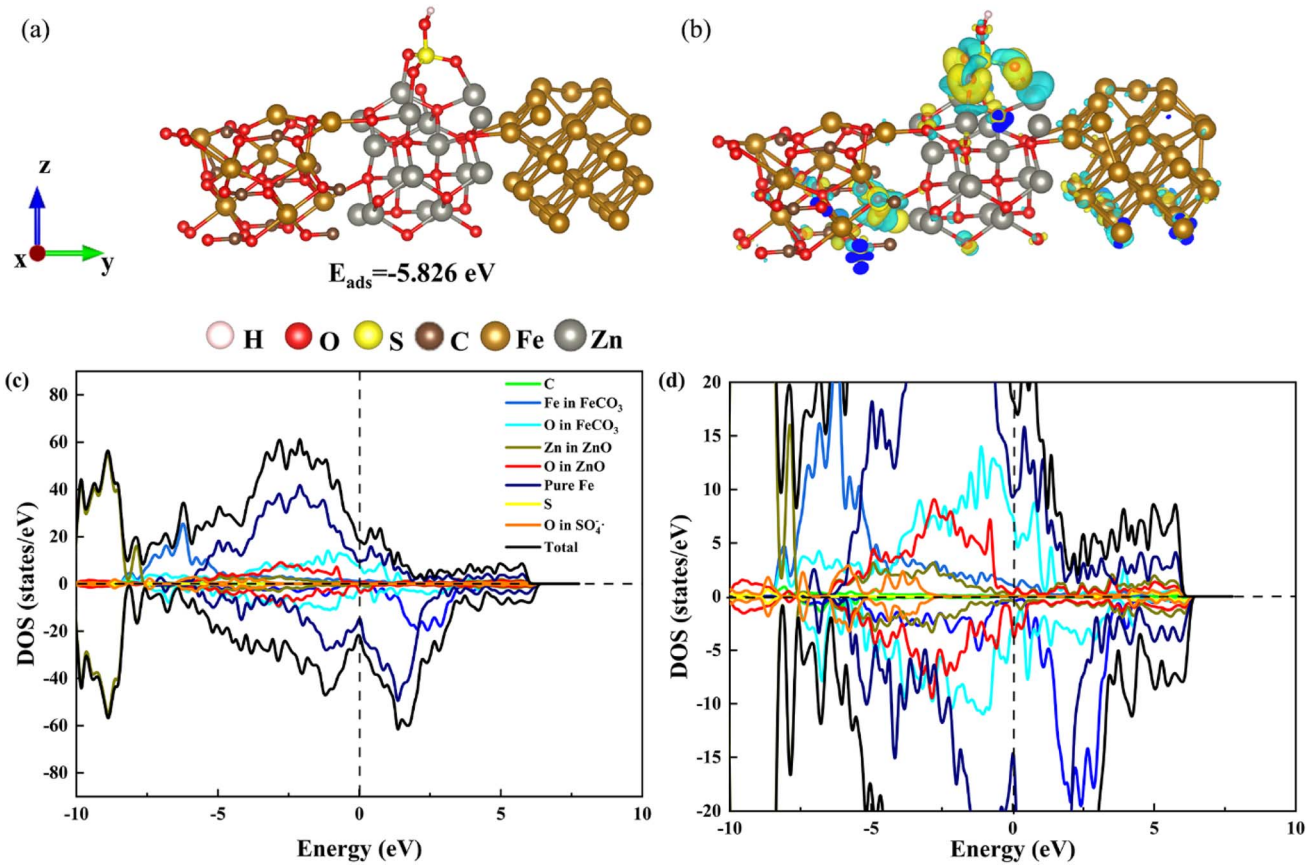

Fig. 6 (a) Adsorption energy of FZ13; (b) DCD of FZ13; (c) DOS of FZ13; (d) is an enlarged view of (c).

3.3.4 Possible reaction mechanism in the FZ13 + PMS + light system. The proposed reaction mechanism is based on a comprehensive analysis from various perspectives, including characterization, catalytic performance evaluation, ROS identification and non-radical pathways, electrochemical tests, and DFT calculations.

The FZ13 catalyst was synthesized using α-Fe_2O_3 modified by introducing a Zn precursor. FZ13 exhibits a heterojunction structure and abundant reactive sites, which enhance the system's electron transfer efficiency and charge transfer capacity. This results in a high redox ability within the system, ensuring that the reaction process occurs effectively. In the FZ13 + PMS + light system, photogenerated e^- and h^+ are produced at the heterojunction interface of FZ13 under visible light irradiation. Simultaneously, FZ13 and PMS interact to form the FZ13/PMS* complex. The electrons accumulate in the conduction band (CB), effectively trapping O_2 to generate $O_2^{\cdot-}$, which is further converted into $^1O_2$. The strong oxidative h^+ in the valence band (VB) and H_2O/OH^- form $^{\cdot}OH$. Additionally, FZ13 in the system contains various low-valence states, such as $Fe^0/Fe^{2+}/Zn^{2+}$, which can activate PMS to produce $SO_4^{\cdot-}$, $^{\cdot}OH$, and $Fe^{2+}/Fe^{3+}/Zn^{3+}$. The resulting hypervalent $Fe^{2+}/Fe^{3+}/Zn^{3+}$ acts as an electron trap center, capturing light-induced electrons and being reduced back to $Fe^0/Fe^{2+}/Zn^{2+}$, thus maintaining internal electron balance. The generated ROS ($SO_4^{\cdot-}$, $^{\cdot}OH$, and $O_2^{\cdot-}$) and non-radical species (h^+, e^-, and $^1O_2$) then directly interact with TC molecules. Ultimately, TC is degraded into small molecules, H_2O, and CO_2, as shown in Fig. 7 and described by eqn (1)–(8).

$$FZ13 + h\nu \rightarrow e_{(CB)}^- + h_{(VB)}^+ \quad (1)$$

$$FZ13 + PMS \rightarrow FZ13/PMS^* \quad (2)$$

$$O_2 + e_{(CB)}^- \rightarrow O_2^{\cdot-} \quad (3)$$

$$O_2^{\cdot-} + h_{(VB)}^+ \rightarrow {}^1O_2 \quad (4)$$

$$h_{(VB)}^+ + H_2O/OH^- \rightarrow {}^{\cdot}OH \quad (5)$$

$$Fe^0/Fe^{2+}/Zn^{2+} + HSO_5^- \rightarrow Fe^{2+}/Fe^{3+}/Zn^{3+} + SO_4^{\cdot-} + H^+ \quad (6)$$

$$Fe^{2+}/Fe^{3+}/Zn^{3+} + e_{(CB)}^- \rightarrow Fe^0/Fe^{2+}/Zn^{2+} \quad (7)$$

$$SO_4^{\cdot-}/{}^{\cdot}OH/O_2^{\cdot-}/h^+/e^-/{}^1O_2 + TC \rightarrow \text{small molecules} + CO_2 + H_2O \quad (8)$$

3.4 Degradation performance in the FZ13 + PMS + light system

3.4.1 Applicability of the FZ13 + PMS + light system. As shown in Fig. S10(a),† the degradation efficiency of TC is not inhibited—and even slightly enhanced—under weakly to

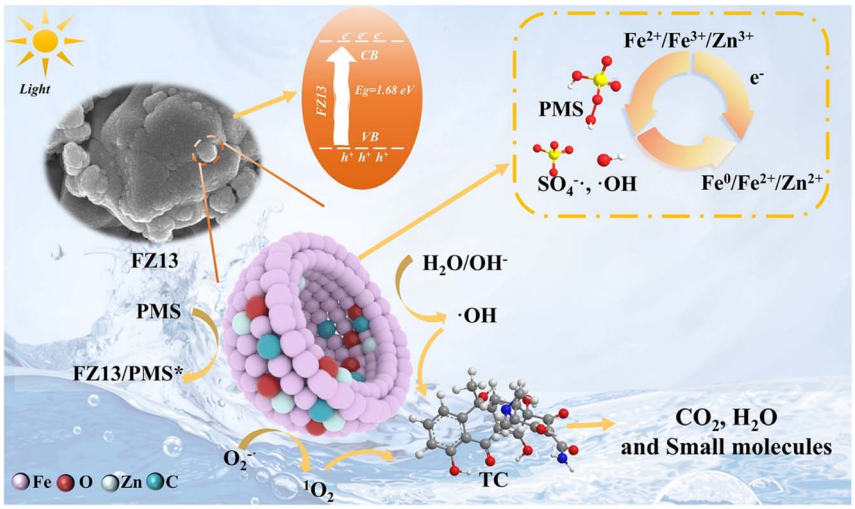

Fig. 7 Reaction mechanism diagram of the FZ13 + PMS + light system.

strongly alkaline conditions. In contrast, a slight decrease in degradation efficiency is observed at pH 1 and pH 3. Zeta potential analysis (Fig. S11†) reveals that the point of zero charge (pH_{PZC}) of FZ13 is 9.53. Under acidic conditions, HSO_5^- remains relatively stable, and its reaction kinetics with FZ13 is suppressed, leading to reduced TC degradation. At strongly alkaline pH levels (pH = 13), electrostatic repulsion between negatively charged HSO_5^- and the FZ13 surface inhibits the formation of FZ13/PMS* complexes, thereby reducing catalytic activity and ultimately lowering TC degradation efficiency.[7] Additionally, the impact of various interfering substances (Cl^-, SO_4^{2-}, $H_2PO_4^-$, NO_3^-, HCO_3^-, and HA) on TC degradation efficiency is explored, as shown in Fig. S10(b) and (c).† Although differences are observed in their efficiencies, these substances have minimal effects on TC degradation, indicating that the FZ13 + PMS + light system has strong environmental applicability in wastewater treatment.

Considering the diversity of actual wastewater pollutants and water quality, the universality of the FZ13 + PMS + light system was further examined (Fig. S10(d) and (e)†). Levofloxacin (LEVF), rhodamine B (RhB) and methylene blue (MB) were degraded by 72.4%, 84.5% and 93.8%, respectively. Meanwhile, the degradation of TC was not affected by the water quality of lake water or tap water, further confirming the superior applicability of the FZ13 + PMS + light system.

Additionally, the real situation of the FZ13 + PMS + light system was evaluated through medical wastewater. The degradation efficiencies of COD, TOC and NH_3^-N within 90 min were 64.7%, 37.1% and 56.9% respectively (Fig. S12†). The original data are shown in Table S5.†

3.4.2 Possible degradation pathways and toxicological analysis of the FZ13 + PMS + light system. The possible degradation pathways and intermediates of TC were identified through LC-MS, as shown in Fig. S13.† In pathway 1, TC molecules (m/z = 445) undergo deamination to form P1 (m/z = 392), followed by a ring-opening reaction and reduction to P2 (m/z = 350) and P3 (m/z = 218). In pathway 2, the C–N bond of TC (m/z = 445) undergoes demethylation to form P4, which is subsequently dehydroxylated to form P5 (m/z = 396). In pathway 3, TC is hydroxylated to produce intermediate P6 (m/z = 475), and dehydration converts P6 to P7 (m/z = 431).

The possible transfer pathway of organic matter before and after TC degradation in the FZ13 + PMS + light system was verified using 3D-EEM, as shown in Fig. S14(a) and (b).† The fluorescence peak area significantly decreases after the reaction, with the fluorescence shifting from zones IV and V to zone IV. This is due to the degradation of humic acid substances in TC, which are transformed into soluble microbial byproducts, leading to weakened fluorescence intensity. This observation indicates effective TC degradation, which is also reflected in the decrease in TOC.

To evaluate the environmental safety of the TC degradation process, the toxicity profiles of TC and its major degradation intermediates (P1–P7) were predicted using the T.E.S.T. As shown in Fig. S15 and detailed in Table S6,† six toxicity indicators were considered: fathead minnow LC_{50} (96 h), *Daphnia magna* LC_{50} (48 h), oral rat LD_{50}, bioconcentration factor (BCF), developmental toxicity, and mutagenicity. From the aquatic toxicity perspective, all intermediates exhibit significantly higher LC_{50} values compared to TC (0.9 for fathead minnow and 5.44 for *Daphnia magna*), indicating reduced acute toxicity. For instance, P1 and P6 show fathead minnow LC_{50} values of 59.45 and 83.22, and *Daphnia magna* LC_{50} values of 103.00 and 173.83, respectively. In terms of mammalian toxicity, oral rat LD_{50} values for most intermediates exceed that of TC (1524.04), suggesting reduced systemic toxicity. P1 and P5 exhibit LD_{50} values of 1881.66 and 2930.77, respectively. Although P3 shows a slightly lower LD_{50} (1038.53), it remains within a comparable toxicity range. The bioconcentration factor of TC is low (0.71), and while some intermediates display higher BCFs (P1: 12.66; P4: 6.65), they remain relatively low, indicating minimal bioaccumulation risk. Regarding chronic toxicity endpoints, such as developmental toxicity and mutagenicity, most intermediates show comparable or reduced levels relative to TC. For example,

P3 exhibits a lower mutagenicity score (0.44) than TC (0.60), while P5 shows a slight increase (0.82), but within a tolerable range. Developmental toxicity values fluctuate slightly, but no persistent or significantly enhanced toxicity is observed. Moreover, LC-MS analysis confirmed that these intermediates appear only transiently during the degradation process and do not accumulate to high concentrations. Therefore, the overall toxicity of the FZ13 + PMS + light system decreases over time, ensuring that the degradation pathway is both effective and environmentally benign.

4. Conclusions

In this study, the FZ13 catalyst with high catalytic activity and abundant active sites was synthesized, and the degradation of TC by activating PMS under visible light was investigated. The results confirm that the degradation efficiency of TC in the FZ13 + PMS + light system reaches 84%, with a rate constant k of 0.0642 min^{-1}, which is 1.6 times higher than that of the unmodified α-Fe_2O_3 system. DFT calculations reveal that the characteristic peak of FZ13 is further from the Fermi level, indicating better stability. The heterojunction structure of FZ13 forms Fe–O–Zn bonds, which not only enhance electron transport efficiency but also improve the separation of photogenerated electron–hole pairs. Meanwhile, forming the FZ13/PMS* complex in the FZ13 + PMS + light system facilitates rapid electron transfer. $SO_4^{\bullet-}$, $^{\bullet}OH$, $O_2^{\bullet-}$, h^+, e^- and $^1O_2$ are co-involved in the degradation of TC. This study provides an effective strategy for the preparation of materials for photo-assisted activation of PMS.

Data availability

Data available on request from the authors.

Conflicts of interest

The authors declare that they have no known competing financial interests or personal relationships that could have appeared to influence the work reported in this paper.

References

1 Z. Wang, Z. Yi, L. W. Wong, X. Tang, H. Wang, H. Wang, C. Zhou, Y. He, W. Xiong, G. Wang, G. Zeng, J. Zhao and P. Xu, *Adv. Mater.*, 2024, **36**, 2404278.
2 P. Chen, X. Zhang, Z. Cheng, Q. Xu, X. Zhang, Y. Liu and F. Qiu, *J. Cleaner Prod.*, 2023, **426**, 139202.
3 Y. Wang, D. Li, X. Ge, J. Yu, Y. Zhao and Y. Bu, *Adv. Mater.*, 2024, **36**, 2402935.
4 S. Zhang, C. Lu, Y. Wang, C. Tian, P. Chen, M. Yang, M. Zhang, R. Xu, Y. He and Z. Li, *J. Cleaner Prod.*, 2024, **434**, 140384.
5 L. Yang, Z. Xiong, J. Li, Z. Wu, X. Zhao, C. Zhao, Y. Zhou, Y. Qian and B. Lai, *Chem. Eng. J.*, 2022, **444**, 136623.
6 H. Liu, Y. Fu, S. Chen, W. Zhang, K. Xiang, F. Shen, R. Xiao, L. Chai and F. Zhao, *Chem. Eng. J.*, 2023, **474**, 145571.
7 P. Chen, Z. Cheng, X. Zhang, C. Yan, J. Wei, F. Qiu and Y. Liu, *J. Cleaner Prod.*, 2024, **445**, 141365.
8 Y. He, H. Qin, Z. Wang, H. Wang, Y. Zhu, C. Zhou, Y. Zeng, Y. Li, P. Xu and G. Zeng, *Appl. Catal., B*, 2024, **340**, 123204.
9 Q. Wang, Z. Guan, S. Ding, D. Xia and D. Li, *Sep. Purif. Technol.*, 2022, **289**, 120625.
10 Y. Gao, Y. Chen, T. Song, R. Su and J. Luo, *Sep. Purif. Technol.*, 2022, **300**, 121857.
11 S. Pan, X. Guo, X. Lu, R. Li, H. Hu, X. Nie, B. Liu, R. Chen, M. Zhu, S. Hei, X. Zhu, S. Zhang and H. Zhou, *Appl. Catal., B*, 2023, **330**, 122508.
12 J. Zhang, H. Zeng, L. Bu, S. Zhou, Z. Shi and L. Deng, *Chem. Eng. J.*, 2023, **454**, 139989.
13 J. Song, N. Hou, X. Liu, M. Antonietti, P. Zhang, R. Ding, L. Song, Y. Wang and Y. Mu, *Adv. Mater.*, 2023, **35**, 2209552.
14 A. Wang, R. Wang, Y. Pan, J. Ni, X. Liang, M. Du, J. Zhang, D. Liu, J. Ma, J. Wang and W. Wang, *Appl. Catal., B*, 2024, **344**, 123621.
15 Y. Liu, F. Cun, D. Tian, P. Zhou, Y. Yuan, Z. Xiong, C. He, Y. Du, Z. Pan and B. Lai, *J. Hazard. Mater.*, 2022, **435**, 128975.
16 A. Wang, P. Zhou, D. Tian, H. Zhang, Z. Xiong, Y. Du, C. He, Y. Yuan, T. Chen, Y. Liu and B. Lai, *Appl. Catal., B*, 2022, **316**, 121631.
17 Y. Deng, J. Wang, J. Wang, H. Zhang, H. Xiao, C. Zhang and W. L. Wang, *Appl. Catal., B*, 2023, **338**, 123041.
18 H. Cai, Y. Niu, T. Guan, Y. Zhang and Z. Ma, *J. Environ. Manage.*, 2024, **364**, 121431.
19 Y. Zhang, R. Huang, Y. Fang, J. Wang, Z. Yuan, X. Chen, W. Zhu, Y. Cai and X. Shi, *Sep. Purif. Technol.*, 2024, **336**, 126164.
20 T. Li, Y. Liu, M. Li, J. Jiang, J. Gao and S. Dong, *Sep. Purif. Technol.*, 2021, **266**, 118605.
21 H. Sun, S. Liu, S. Liu and S. Wang, *Appl. Catal., B*, 2014, **146**, 162–168.
22 Z. Jia, Y. Yang, C. Yang and D. Wang, *Appl. Surf. Sci.*, 2024, **659**, 159866.
23 F. Hayati, S. Moradi, S. F. Saei, Z. Madani, S. Giannakis, A. A. Isari and B. Kakavandi, *J. Environ. Manage.*, 2022, **321**, 115851.
24 J. Wang, Q. Zhang, Y. Li, C. Gao, L. Jiang and X. Wu, *Chem. Eng. J.*, 2024, **483**, 149259.
25 X. Dou, Y. Chen and H. Shi, *Chem. Eng. J.*, 2022, **431**, 134054.
26 J. Li, D. Wang, S. Zhao, R. Ma, J. Guo, Z. Li, D. Wang, Y. Xuan and L. Wang, *Appl. Catal., B*, 2024, **351**, 124007.
27 D. Terrón, J. P. Holgado-Vázquez, A. Giráldez, E. Rosales, M. A. Sanromán and M. Pazos, *J. Environ. Chem. Eng.*, 2024, **12**, 113403.
28 K. Zhang, D. Huang, Y. Zhang, N. E. H. Bouroubi, P. Chen, N. Ganbold, P. He, J. Liu, Y. Fang, M. Gan, J. Zhu and B. Yang, *J. Environ. Manage.*, 2023, **335**, 117540.
29 Z. Wang, C. Lai, L. Qin, Y. Fu, J. He, D. Huang, B. Li, M. Zhang, S. Liu, L. Li, W. Zhang, H. Yi, X. Liu and X. Zhou, *Chem. Eng. J.*, 2020, **392**, 124851.
30 X. Li, T. Chen, Y. Qiu, Z. Zhu, H. Zhang and D. Yin, *Chem. Eng. J.*, 2023, **452**, 139659.
31 H. Zhou, L. Xiao, Y. Deng, C. Chen, X. Pei, Q. Li, Y. Ye and F. Pan, *Chem. Eng. J.*, 2023, **471**, 144685.

32 W. An, H. Wang, T. Yang, J. Xu, Y. Wang, D. Liu, J. Hu, W. Cui and Y. Liang, *Chem. Eng. J.*, 2023, **451**, 138653.
33 T. Wang, J. Zheng, J. Cai, Q. Liu and X. Zhang, *Sci. Total Environ.*, 2022, **839**, 155955.
34 H. Ming, P. Zhang, Y. Yang, Y. Zou, C. Yang, Y. Hou, K. Ding, J. Zhang and X. Wang, *Appl. Catal., B*, 2022, **311**, 121341.
35 Z. Shen, Z. Zhu, G. Wang, Z. Wang, W. Chen and W. Lu, *J. Solid State Chem.*, 2023, **319**, 123806.
36 T. Li, M. Li, J. Jiang, Z. Zhao, Z. Li, C. Zhao, X. Wang and S. Dong, *Appl. Catal., B*, 2023, **330**, 122539.
37 X. Zhang, C. Li, L. Dai, C. Si, Z. Shen, Z. Qiu and J. Wang, *J. Environ. Chem. Eng.*, 2023, **11**, 110869.
38 P. Chen, Z. Cheng, L. Zhang, S. Tan, J. Sun, J. Wang, F. Duan, A. Du and S. Li, *J. Water Process Eng.*, 2024, **62**, 105328.
39 P. Chen, L. Zhang, Z. Cheng, J. Tang, H. Huang, C. Jian and Z. Wei, *Crystals*, 2023, **13**, 1248.
40 X. Zhang, X. Xu, C. Li, Z. Hao, J. Yu, H. He, C. Si, Z. Shen, Z. Qiu and J. Wang, *Adv. Compos. Hybrid Mater.*, 2023, **6**, 145.
41 M. Du, H. Zhang, S. Dong, B. Wang and Y. Zhang, *Sep. Purif. Technol.*, 2024, **335**, 126175.
42 P. Shao, Y. Jing, X. Duan, H. Lin, L. Yang, W. Ren, F. Deng, B. Li, X. Luo and S. Wang, *Environ. Sci. Technol.*, 2021, **55**, 16078–16087.
43 H. Chen, X. Zhang, L. Jiang, X. Yuan, J. Liang, J. Zhang, H. Yu, W. Chu, Z. Wu, H. Li and Y. Li, *Sep. Purif. Technol.*, 2021, **272**, 118947.
44 H. Ming, D. Wei, Y. Yang, B. Chen, C. Yang, J. Zhang and Y. Hou, *Chem. Eng. J.*, 2021, **424**, 130296.
45 G. Di, Z. Zhu, H. Zhang, J. Zhu, H. Lu, W. Zhang, Y. Qiu, L. Zhu and S. Küppers, *Chem. Eng. J.*, 2017, **328**, 141–151.
46 S. Wang, S. Gai, K. Cheng, Z. Liu, M. Antonietti and F. Yang, *Sep. Purif. Technol.*, 2025, **359**, 130541.
47 Y. Chai, H. Dai, P. Zhan, Z. Liu, Z. Huang, C. Tan, F. Hu, X. Xu and X. Peng, *J. Hazard. Mater.*, 2023, **452**, 131202.
48 L. Liu, H. He, Y. Fu, C. Xu, X. Xia, X. Hu and H. Liao, *Mater. Lett.*, 2023, **351**, 135091.
49 Y. Jia, L. Duan, H. Li, C. Zhang, Q. Gao, H. Zhang, S. Li and M. Li, *Sep. Purif. Technol.*, 2025, **354**, 129287.
50 Y. Shen, M. J. Martín de Vidales, G. Gorni, M. J. Sampaio, A. M. T. Silva, A. R. Lado Ribeiro and A. J. Dos santos-García, *Appl. Catal., B*, 2024, **357**, 124291.
51 J. Song, N. Hou, X. Liu, G. Bi, Y. Wang and Y. Mu, *Adv. Mater.*, 2024, **36**, 2405832.
52 Y. Chai, H. Dai, X. Duan, Z. Sun, F. Hu, J. Qian and X. Peng, *Appl. Catal., B*, 2024, **341**, 123289.
53 Y. Ma, D. Wang, Y. Xu, H. Lin and H. Zhang, *J. Hazard. Mater.*, 2022, **436**, 129172.
54 X. Guo, Q. Zhang, H. He, A. Cai, S. Xi, J. Du, F. Zhang, X. Fan, W. Peng and Y. Li, *Appl. Catal., B*, 2023, **335**, 122886.
55 B. C. Sun, W. K. Zhao, C. B. Han, J. Y. Zheng, H. Yan, Z. C. Yang, L. Sun, X. Wang and X. Song, *J. Alloys Compd.*, 2023, **942**, 169037.
56 B. He, L. Song, Z. Zhao, W. Liu, Y. Zhou, J. Shang and X. Cheng, *Chem. Eng. J.*, 2022, **446**, 137183.
57 Y. Wang, Y. Sun, R. Wang, M. Gao, Y. Xin, G. Zhang, P. Xu and D. Ma, *J. Hazard. Mater.*, 2023, **451**, 130901.
58 J. Guo, C. Ding, W. Gan, P. Chen, Y. Lu, J. Li, R. Chen, M. Zhang and Z. Sun, *Sep. Purif. Technol.*, 2023, **307**, 122838.